

1 **Bayesian performance evaluation of evapotranspiration models: a case study based on** 2 **eddy covariance system of a maize field in northwestern China**

3 Guoxiao Wei ^{1,2}, Xiaoying Zhang ^{3,*}, Ming Ye ⁴, Ning Yue ^{1,2}, Fei Kan ^{1,2}

4 ¹ Key Laboratory of Western China's Environmental System (Ministry of Education), Lanzhou University,
5 China, 730000

6 ² School of Earth and Environmental Sciences, Lanzhou University, China, 730000

7 ³ Construct Engineering College, Jilin University, China, 130400

8 ⁴ Department of Earth, Ocean, and Atmospheric Science, Florida State University, USA, 32306

9 * Corresponding author: xiaoyingzh@jlu.edu.cn.

10 **Abstract**

11 Evapotranspiration (ET) is a major component of the land surface process involved in energy fluxes and energy
12 balance, especially in the hydrological cycle of agricultural ecosystems. While many models have been
13 developed as powerful tools to estimate ET, there is no agreement on which model best describing the loss of
14 water to the atmosphere. In this study, we present a solid study to evaluate four widely used ET models and their
15 parameter contributions using half-hourly ET observations obtained at a spring maize field in an arid region.
16 The four tested models are Shuttleworth Wallace (SW) model, Penman-Monteith (PM) model, Priestley-Taylor
17 and Flint-Childs (PT-FC) model, and Advection-Aridity (AA) model. The parameters in each model were first
18 calibrated using Differential Evolution Adaptive Metropolis (DREAM) algorithm, and then were analyzed to
19 identify their impacts on the model performance. The Bayesian model evidence (BME) approach, was further
20 adopted to select the optimal model by incorporating the mathematically rigorous thermodynamic integration
21 algorithm. Our results revealed that the extinction coefficient was the most significant parameter in the ET
22 models. It was not merely partitioning the total available energy into the canopy and surface, but also including
23 the energy imbalance correction. The extinction coefficient is well constrained in the SW model and poorly
24 constrained in the PM model, but not considered in PT-FC and AA models. This is the main reason that the SW
25 model outperforming the other models. Although the SW model with seven parameters is sophisticated, it's
26 good fitting to observations can counterbalance its higher complexity. In addition, the discrepancies between
27 observations and model simulations were evaluated using traditional error metrics. The mismatch analysis
28 indicated that explicit treatment of energy imbalance and energy interaction will be the primary way to further
29 improve ET model performance.

30 **Keywords:** Bayesian analysis; ET models; Eddy covariance; Model performance; Extinction coefficient

31 **1. Introduction**

32 Surface energy fluxes are an important component of Earth's global energy budget and a primary
33 determinant of surface climate. Evapotranspiration (ET), as a major energy flux process for energy balance,
34 accounts for about 60-65% of the average precipitation over the surface of the Earth (Brutsaert, 2005). In
35 agricultural ecosystems, more than 90% of the total water losses are due to ET (Morison et al., 2008). Therefore,
36 robust ET estimation is crucial to a wide range of problems in hydrology, ecology, and global climate change
37 (Xu and Singh, 1998). In practice, much of our understanding of how land surface processes and vegetation
38 affect weather and climate is based on numerical modeling of surface energy fluxes and the
39 atmospherically-coupled hydrological cycle (Bonan, 2008). Several models are commonly used in agricultural
40 systems to evaluate ET. The Penman-Monteith (PM) and Shuttleworth-Wallace (SW) models are physically
41 sound and rigorous (Zhu et al., 2013), and thus widely used to estimate ET for seasonally varied vegetations.
42 The models consider the relationships between net radiation, all kinds of heat flux (such as latent heat, sensible
43 heat, and heat from soil and canopy), and surface temperature. The Priestley-Taylor and Flint-Childs (PT-FC)
44 model (based on radiation) and the advection-aridity (AA) model (based on meteorological variables) have also
45 been widely used because they only require a small number of ground-based measurements to set up the models
46 (Ershadi et al., 2014).

47 These ET models are generally complex, because of the coupling of the land surface and atmospheric
48 processes, and high-dimensional with a large number of parameters. Comparing the performance of competing
49 models and evaluating and understanding the discrepancies between simulations of the models and
50 corresponding observed surface-atmosphere water flux are remain challenging problems (Legates, 1999). Both
51 non-Bayesian analysis (Szilagyi and Jozsa, 2008; Vinukollu et al., 2011; Li et al., 2013; Ershadi et al., 2015) and
52 Bayesian analysis have been used to evaluate the performance of ET models (Zhu et al., 2014; Chen et al., 2015;
53 Liu et al., 2016; Zhang et al., 2017; Elshall et al., 2018; Samani et al., 2018; Zeng et al., 2018) . Li et al. (2013)
54 compared the ET simulations of the PM, SW and adjusted SW models under film-mulching conditions of maize
55 growth in an arid region of China. They found that the half-hourly ET was overestimated by 17% by the SW
56 model. In contrast, the PM and adjusted SW models underestimated the daily ET by 6% and 2%, respectively.
57 Therefore, the performances of PM and adjusted SW models are better than that of the SW model in their case

58 study. Ershadi et al. (2014) evaluated the surface energy balance system (SEBS), PM, PT-JPL (a modified
59 Priestley–Taylor model) and AA models. Based on the average value of EF and RMSE, the model ranking from
60 worst to best was AA, PM, SEBS, and PT-JPL. Ershadi et al. (2015) also compared the response of the models
61 to different formulations of aerodynamic and surface resistances with global FLUXNET data. Their results
62 showed considerable variability in model performance among and within biome types. Currently, ET model
63 selection and comparison have been still conducted using traditional error metrics. It is known that error metrics
64 are not adequate to provide reasonable result of model ranking for disregarding model complexity (Marshall et
65 al., 2005; Samani et al., 2018). The focus of this study is to use a Bayesian approach to evaluate the performance
66 of the PM, SW, PT-FC, and AA models, which is a novelty contribution of this study. In ET models, the land
67 surface energy system is governed by presumably infinite-dimensional physics. However, considering the ET
68 models as finite-dimensional can be more precisely by covering all relevant relations. Therefore, employing
69 consistent criteria for model selection might be justified when the aim is to better understand the processes
70 involved (Höge et al., 2018). When using consistent model selection, Bayesian model evidence (BME), also
71 known as marginal likelihood, measures the average fit of model simulations to their corresponding
72 observations over a model’s prior parameter space. This feature enables BME to consider model complexity (in
73 terms of number of model parameters) for model performance evaluation. When comparing several alternative
74 conceptual models, the model with the largest marginal likelihood is selected as the best model (Lartillot and
75 Philippe, 2006). BME can thus be used for evaluating the model fit (over the parameter space) and for
76 comparing alternative models. In previous studies, the Bayesian information criterion (BIC; Schwarz, 1978) and
77 the Kashyap information criterion (KIC; Kashyap, 1982) have been used to approximate BME by using
78 maximum likelihood theories to reduce computational cost of evaluating BME (Ye et al., 2004). However, these
79 approximations have theoretical and computational limitations (Ye et al., 2008; Xie et al., 2011; Schöniger et al.,
80 2014), and a numerical evaluation (not a likelihood approximation) of BME is necessary, especially for complex
81 models (Lartillot and Philippe, 2006). Lartillot and Philippe (2006) advocated the use of thermodynamic
82 integration (TI) for estimating BME, also known as path sampling (Gelman and Meng, 1998; Neal, 2000), in
83 order to avoid sampling solely in the prior or posterior parameter space. TI uses samples that are systematically
84 generated from the prior to the posterior parameter space by conducting path sampling with several discrete
85 power coefficient values (Liu et al., 2016). It is numerically accurate than the generally used harmonic mean
86 method (Xie et al., 2011).

87 Most applications of Bayesian methods have focused on the calibration of individual models, while the
88 comparison of alternative models continues to be performed using traditional error metrics. More generally,
89 Bayesian approaches to model calibration, comparison, and analysis have been used far less used in the
90 evaluation of ET models than in other areas of environmental science. In this study, the Bayesian approach is
91 used to calibrate and evaluate the four ET models (PM, SW, PT-FC, and AA) based on an experiment over a
92 spring maize field in an arid area of northwest China, from 3 June to 27 September 2014. The objectives of the
93 study are as follows: (1) to calibrate ET model parameters using the DiffereRential Evolution Adaptive Metropolis
94 (DREAM) algorithm (Vrugt et al., 2008, 2009); (2) to identify which parameters had a greater impact on the
95 model performance and to explain why the selected optimal model performed best; (3) to evaluate the
96 performance of the models using traditional error metrics and BME; and (4) to analyze discrepancies between
97 model simulations and observation data in order to better understand model performance and identify ways to
98 improve these models. We expect that the study will not only boost the development of model parameterization
99 and model selection but also contribute to the improvement of the ET models.

100 **2. Data and methodology**

101 **2.1. Description of the study area**

102 The experiment of maize growth was conducted at Daman Superstation, located in Zhangye City, Gansu
103 province, northwest China. Daman Oasis is located in the middle Heihe River basin, which is the second largest
104 inland river basin in the arid region of northwest China. The midstream area of the Heihe River basin is
105 characterized by oases with irrigated agriculture, and is a region that consumes large amount of water for both
106 domestic and agricultural uses. The annual average precipitation and temperature are 125 mm and 7.2 °C (1960–
107 2000), respectively. The annual accumulated temperature (>10 °C) is 3,234 °C, and the annual average potential
108 evaporation is about 2,290 mm. The average annual duration of sunshine is 3,106 h with 148 frost-free days.
109 The predominant soil type is silty-clay loam and the depth of the frozen layer is about 143 mm. The study area
110 is a typical irrigated agricultural region, and the major source of water is snowmelt from the Qilian Mountains.
111 Maize and spring wheat are the principal crops grown in the region. Maize is generally sown in late April and
112 harvested in mid-September, and is planted with a row spacing of 40 cm and a plant spacing of 30 cm. The plant
113 density is about 66,000 plants per hectare in the study area.

114 2.2. Measurements and data processing

115 Our data were collected from the field observation systems of the Heihe Watershed Allied Telemetry
116 Experimental Research (HiWATER) project as described in Li et al (2013). The observation period was from
117 DOY (day of the year) 154 to DOY 270 in 2014. An open-path eddy covariance (EC) system was installed in a
118 maize field, with the sensors at a height of 4.5 m. Maize is the main crop in the study region, and thus covers
119 sufficient planting area to set the EC measurements. The EC data was logged at a frequency of 10 Hz and then
120 processed with an average time interval of 30 min. Sensible and latent heat fluxes were computed by the EC
121 approach of Baldocchi (2003). Flux data measured by EC were controlled by traditional methods, including
122 three-dimensional rotation (Aubinet et al., 2000), WPL (Webb-Penman-Leuning) density fluctuation correction
123 (Webb et al., 1980), frequency response correction (Xu et al., 2014), and spurious data removal caused by
124 rainfall, water condensation, and system failure. About 85% of the energy balance closure was observed in the
125 EC data (Liu et al., 2011).

126 Standard hydro-meteorological variables, including rainfall, air temperature, wind speed, and wind
127 direction, were continuously measured at the heights of 3, 5, 10, 15, 20, 30 and 40 m above the ground. Soil
128 temperature and moisture were measured at heights of 2, 4, 10, 20, 40, 80, 120 and 160 cm. Photosynthetically
129 active radiation was measured at a height of 12 m. Net radiation, including downward, upward and longwave
130 radiation, was measured by a four-component net radiometer. An infrared thermometer was installed at a height
131 of 12 m. Leaf Area Index (LAI) was measured approximately every 10 days during the growing season.

132 2.3. Model description

133 In this section, we summarize the mathematical definitions forming the basis of each of the four models.
134 Appendix A contains a summary of the names and physical meanings of the model parameters.

135 2.3.1 Penman-Monteith (PM) model

136 The PM model can be formulated in the following way (Monteith, 1965):

$$137 \lambda E = \frac{\varepsilon A + (\rho C_p / \gamma) D_a g_a}{\varepsilon + 1 + g_a / g_s} \quad (1)$$

138 where $\varepsilon=A/\gamma$; and A is defined to be $A = R_n - G$.

139 In the present study, g_a is parameterized in the way suggested by Leuning (2008) and g_s is defined as:

$$140 \quad g_s = g_s^c \left[\frac{1 + \frac{\tau g_a}{(\varepsilon + 1) g_s^c} \left[f - \frac{(\varepsilon + 1)(1 - f) g_s^c}{g_a} \right] + \frac{g_a}{\varepsilon g_i}}{1 - \tau \left[f - \frac{(\varepsilon + 1)(1 - f) g_s^c}{g_a} \right] + \frac{g_a}{\varepsilon g_i}} \right] \quad (2)$$

141 where $1-\tau$ and τ are the fraction of the total available energy absorbed by the canopy and by the soil, and $\tau = \exp$
 142 $(-K_a LAI)$, and g_i and g_s^c are defined in equations (3) and (4), respectively (Monteith, 1965):

$$143 \quad g_i = \frac{A}{(\rho C_p / \gamma) D_a} \quad (3)$$

$$144 \quad g_s^c = \frac{g_{\max}}{K_q} \ln \left[\frac{Q_h + Q_{50}}{Q_h \exp(-K_q LAI) + Q_{50}} \right] \left[\frac{1}{1 + D_a / D_{50}} \right] f(\theta) \quad (4)$$

145 where $f(\theta)$ represents water stress and is expressed as:

$$146 \quad f(\theta) = \begin{cases} 1 & \theta > \theta_a \\ \frac{\theta - \theta_b}{\theta_a - \theta_b} & \theta_b < \theta < \theta_a \\ 0 & \theta < \theta_b \end{cases} \quad (5)$$

147 and θ_a is set as $\theta_a = 0.75 \theta_b$. Aerodynamic conductance g_a is calculated as:

$$148 \quad g_a = \frac{k^2 u_m}{\ln[(z_m - d)/z_{0m}] \ln[(z_m - d)/z_{0v}]} \quad (6)$$

149 where the quantities d , z_{0m} and z_{0v} are calculated using $d = 2h/3$, $z_{0m} = 0.123h$ and $z_{0v} = 0.1z_{0m}$ (Allen 1998).

150 2.3.2. Shuttleworth-Wallace (SW) model

151 The SW model comprises a one-dimensional model of plant transpiration and a one-dimensional model of
 152 soil evaporation. The two terms are calculated by the following equations:

153 $\lambda E T = \lambda E + \mathcal{A} = C_s E T + C_c E$ (7)

154
$$E T_s = \frac{\Delta A + \{\rho C_p (e_s - e_a) - \Delta r_a^s (A - A_s)\}}{\Delta + \gamma \left\{1 + r_s^s / (r_a^a + r_a^s)\right\}}$$
 (8)

155
$$E T_c = \frac{\Delta A + \{\rho C_p (e_s - e_a) - \Delta r_a^c A\}}{\Delta + \gamma \left\{1 + r_s^c / (r_a^a + r_a^c)\right\}}$$
 (9)

156 where the available energy input above the soil surface is defined as $A_s = R_{ns} - G$.

157 R_{ns} can be calculated using the Beer's law relationship:

158
$$R_{ns} = R_{fl} \times \left[1 - \exp\left(-\frac{K_d L A}{R_{fl}}\right)\right]$$
 (10)

159 The coefficients C_s and C_c are obtained as follows:

160
$$C_s = \left\{1 + R_s R_a / R_c (R_s + R_a)\right\}^{-1}$$
 (11)

161
$$C_c = \left\{1 + R_c R_a / R_s (R_c + R_a)\right\}^{-1}$$
 (12)

162 where

163
$$R_a = (\Delta + \gamma) r_a^a$$
 (13)

164
$$R_s = (\Delta + \gamma) r_a^s + \gamma r_s^s$$
 (14)

165
$$R_c = (\Delta + \gamma) r_a^c + \gamma r_s^c$$
 (15)

166 Soil surface resistance is expressed as:

167
$$r_s^s = \exp\left[-\frac{\theta}{b_2 \theta_s}\right]$$
 (16)

168 In this study, we consider the reciprocal of bulk stomatal resistance, known as canopy conductance. The

169 calculation of g_s^c is the same as in the PM model. The two aerodynamic resistances (r_a^a and r_a^s) and the

170 boundary layer resistance (r_a^c) are modeled following the approach proposed by Shuttleworth and Gurney

171 (1990).

172 2.3.3. Priestley–Taylor and Flint-Childs (PT-FC) model

173 The Priestley-Taylor model (Priestley and Taylor, 1972) was introduced to estimate evaporation from an
174 extensive wet surface under conditions of minimum advection (Stannard, 1993; Sumner and Jacobs, 2005). The
175 ET is expressed as:

$$176 \quad \lambda ET = \alpha_{PT} \frac{\Delta}{\Delta + \gamma} (R_n - G) \quad (17)$$

177 where α_{PT} is a unitless coefficient. The Priestley-Taylor model was modified by Flint and Childs (1991) in order
178 to scale the Priestley-Taylor potential ET to actual ET for nonpotential conditions (hereafter the PT-FC model):

$$179 \quad \lambda ET = \alpha \frac{\Delta}{\Delta + \gamma} (R_n - G) \quad (18)$$

180 where α is as a function of the environmental variables, which could be related to any process that limits ET
181 (e.g., soil hydraulic resistance, aerodynamic resistance, stomatal resistance); however, only soil moisture status
182 was considered to simplify ET estimation in the PT-FC model (Flint and Childs, 1991). In this model, α is
183 defined as:

$$184 \quad \alpha = \beta_1 [1 - \exp(-\beta_2 \Theta)] \quad (19)$$

185 where $\Theta = \frac{\theta - \theta_r}{\theta_s - \theta_r}$.

186 2.3.4. Advection-aridity (AA) model

187 The AA model was first proposed by Brutsaert and Stricker (1979) and further improved by Parlange and
188 Katul (1992). The model relies on the feedback between actual (λET) and potential ET , which assumes that
189 actual potential ET should converge to wet surface ET at wet surface conditions. Its general form is:

$$190 \quad \lambda ET = (2\alpha_{PT} - 1) \frac{\Delta}{\Delta + \gamma} (R_n - G) - \frac{\gamma}{\Delta + \gamma} \frac{\rho(q^* - q)}{r_a} \quad (20)$$

191 where α_{PT} is the Priestley-Taylor coefficient, usually taken as 1.26 (Priestley and Taylor, 1972); and r_a is similar
 192 to that used for the Penman-Monteith model (Brutsaert and Stricker, 1979; Brutsaert, 2005; Ershadi et al., 2014).
 193 This model is based mainly on meteorological variables and does not require any information related to soil
 194 moisture, canopy resistance or other measures of aridity (Ershadi et al., 2014). In this study, as for the PT-FC
 195 model, we changed α_{PT} to α , which is calculated using the same equation as in the PT-FC model.

196 **2.4 BME Estimation**

197 The Bayesian model evidence (BME) of a model, M , is defined as (Schöniger et al., 2014):

$$198 \quad \text{BME} = p(\mathbf{D}|M) = \int p(\mathbf{D}|\boldsymbol{\theta}, M) p(\boldsymbol{\theta}|M) d\boldsymbol{\theta} \quad (21)$$

199 where \mathbf{D} is observed or estimated data, $\boldsymbol{\theta}$ is the vector of parameters associated with model M , $p(\boldsymbol{\theta}|M)$ is
 200 the prior density of $\boldsymbol{\theta}$ under model M , $p(\mathbf{D}|\boldsymbol{\theta}, M)$ is the joint likelihood of model M and its parameters $\boldsymbol{\theta}$.
 201 Estimating BME using power posterior estimators such as thermodynamic integration (TI) (Lartillot and
 202 Philippe, 2006) depends mainly on the calculation of the marginal likelihood $p(\mathbf{D}|M)$. The main idea of power
 203 posterior sampling is to define a path that links the prior to the unnormalized posterior. Thus, using an
 204 unnormalized power posterior density

$$205 \quad q_\beta(\boldsymbol{\theta}) = p(\mathbf{D}|\boldsymbol{\theta}, M)^\beta p(\boldsymbol{\theta}|M) \quad (22)$$

206 the power coefficient $\beta \in [0, 1]$ is a scalar parameter for discretizing a continuous and differentiable path
 207 linking two unnormalized power posterior densities. The unnormalized power posterior density $q_\beta(\boldsymbol{\theta})$ in
 208 Equation (22) uses the normalizing constant Z_β to yield the normalized power posterior density:

$$209 \quad p_\beta(\boldsymbol{\theta}) = \frac{q_\beta(\boldsymbol{\theta})}{Z_\beta} \quad (23)$$

210 such that

$$211 \quad Z_\beta = \int q_\beta(\boldsymbol{\theta}) d\boldsymbol{\theta} \quad (24)$$

212 The above integral takes a simplified form by the potential:

$$213 \quad U(\boldsymbol{\theta}) = \frac{\partial \ln q_{\beta}(\boldsymbol{\theta})}{\partial \beta} \quad (25)$$

214 thus, the integral can be directly estimated by the following way:

$$215 \quad p(\mathbf{D}|M) = \frac{Z_1}{Z_0} = \exp \left\{ \int_0^1 E_{\theta} [\ln p(\mathbf{D}|\boldsymbol{\theta}, M)] d\beta \right\} \quad (26)$$

216 The one-dimensional integral with respect to β is evaluated by using numerical methods by discretizing β into a
 217 set of β_k . Since there is no theoretical method for selecting β_k values (Liu et al., 2016), we determined these
 218 values using an empirical but straightforward method. Following Xie et al. (2011), a schedule of the power
 219 posterior coefficients β_k is generated by

$$220 \quad \beta_k = (k / K)^{1/\varepsilon} \quad (27)$$

221 for $k=0, 1, 2, \dots, K$. Using $\varepsilon = 0.3$ and $K = 20$ is a reasonable initial choice. By using the trapezoidal rule of
 222 numerical inregration, equation (26) is evaluated via

$$223 \quad p(\mathbf{D}|M) = \exp \left(\int_0^1 y_{\beta} d\beta \right) = \exp \left(\sum_{k=0}^K r_{TI,k} \right) \quad (28)$$

224 such that

$$225 \quad r_{TI,k} = (\beta_k - \beta_{k-1}) \left[\frac{y_k - y_{k-1}}{2} \right] \quad (29)$$

226 and

$$227 \quad y_k = E_{\beta} [\log p(\mathbf{D}|\boldsymbol{\theta}_k, M)] = \frac{1}{n} \sum_{i=1}^n \log p(\mathbf{D}|\boldsymbol{\theta}_{k,i}, M) \quad (30)$$

228 where n is the number of random samples of $\boldsymbol{\theta}_k$ corresponding to β_k , and $\boldsymbol{\theta}_{k,i}$ is the i -th sample.

229 The random samples, $\boldsymbol{\theta}_{k,i}$, are drawn by using the MCMC method implemented in the DREAM code. See
 230 Appendix B for further details on Bayesian inference and the DREAM algorithm. In the DREAM-based
 231 calculation, the Metropolis acceptance ratio is $\alpha_k = \min \left(1, [\alpha_{k, power-posterior} \alpha_{k, prior}] \right)$ with the power

232 posterior ratio given by $\alpha_{k,power-posterior} = (\alpha_{k,prior})^{\beta_k}$. The prior probability ratio
 233 $\alpha_{k,prior} = \Pr(\theta_{k,new} | M) / \Pr(\theta_{k,old} | M)$ is the ratio of the probability of the newly proposed sample
 234 $\theta_{k,new}$ and the probability of the previously accepted sample $\theta_{k,old}$. The posterior probability ratio
 235 $\alpha_{k,prior} = L(\mathbf{D} | \theta_{k,new}, M) / L(\mathbf{D} | \theta_{k,old}, M)$ is the likelihood ratio of samples $\theta_{k,new}$ and $\theta_{k,old}$, and
 236 β_k is the power posterior coefficient. Thus, to use the DREAM algorithm to sample any power posterior
 237 distribution, the regular Metropolis acceptance ratio $\alpha = \min(1, [\alpha_{posterior} \alpha_{prior}])$ is changed to
 238 $\alpha_k = \min(1, [\alpha_{k,power-posterior} \alpha_{k,prior}])$ in DREAM.

239 2.5 Traditional statistical metrics of evaluating model performance

240 The traditional error metrics for evaluating model performance include R^2 and slope (correlation-based
 241 measures), index of agreement (IA) and model efficiency (EF) (relative error measures), and the root mean
 242 square error (RMSE) and mean bias error (MBE) (Poblete-Echeverria and Ortega-Farias, 2009). The definitions
 243 of the listed metrics are:

$$244 \quad IA = 1 - \frac{\sum_{t=1}^n [O(t) - M(t)]^2}{\sum_{t=1}^n [|O(t) - \overline{O(t)}| + |O(t) - \overline{M(t)}|]^2} \quad (31)$$

$$245 \quad EF = 1 - \frac{\sum_{t=1}^n [O(t) - M(t)]^2}{\sum_{t=1}^n [O(t) - \overline{O(t)}]^2} \quad (32)$$

$$246 \quad RMSE = \sqrt{\frac{1}{n} \sum_{t=1}^n [O(t) - M(t)]^2} \quad (33)$$

$$247 \quad MBE = \frac{1}{n} \sum_{t=1}^n [O(t) - M(t)] \quad (34)$$

248 where $O(t)$ is the observation and $\overline{O(t)}$ is the mean observation at time t ; $M(t)$ is the modeled value and
 249 $\overline{M(t)}$ is the mean modeled value estimated by the posterior median parameter values; and n is the total number

250 of the observed values.

251 3. Results

252 3.1 Parameter estimation

253 The PM model has five parameters g_{max} , D_{50} , Q_{50} , K_q and K_a ; the SW model has seven parameters – the five
254 used in the PM model and parameters b_1 and b_2 . The PT-FC and AA models each include two parameters,
255 denoted by β_1 and β_2 (Table 1). The prior probability density of each parameter is specified as a uniform
256 distribution with the ranges listed in Table 1. A total of 50,000 realizations were generated with the DREAM
257 algorithm, which was used to estimate the posterior probability density function of each parameter with the
258 calibration period data from DOY 154 to DOY 202. In the calculations, the chain number, N , was equal to the
259 number of parameters in the associated model. Therefore, N is equal to 5, 7, 2 and 2 for the PM, SW, PT-FC and
260 AA models, respectively. For each model, the first 10,000 samples were discarded as burn-in data, and the
261 remaining 40,000 samples were used for calibration. In total, $40,000 \times N$ realizations were used to set up
262 posterior density functions for each model. To illustrate the efficiency and convergence of DREAM for the ET
263 models, Figure 1 shows the trace plots of the G-R statistic for each of the different parameters in the PM and
264 SW models using a different color. The algorithm required about 8,000 generations to make the G-R statistic
265 close to 1.0 for the two models. The acceptance rates for the PM and SW models were about 15.3% and 18.9%,
266 respectively.

267 Histograms of the DREAM-derived marginal distributions of the parameters are presented in Figure 2 and
268 summarized in Table 2 by Maximum Likelihood Estimates (MLEs), posterior medians and 95% probability
269 intervals. Figures 2a-2e, 2f-2l, 2m-2n, and 2o-2p show histograms of the PM, SW, PT-FC and AA models,
270 respectively. Parameter g_{max} (Fig. 2a) in the PM model, parameters g_{max} , K_a , b_2 (Fig. 2f, 2j, 2l) in the SW model,
271 and parameter β_1 (Fig. 2m) in the PT-FC model and AA model (Fig. 2o) were well constrained and occupied a
272 relatively small range. These parameters displayed a unimodal distribution and appeared approximately
273 Gaussian. In contrast, the distributions of the other parameters differed significantly from a Gaussian
274 distribution, as shown by the corresponding histograms. The distributions of all but one of these parameters
275 concentrated most of the probability mass at their upper limits. The exception was parameter b_1 for the SW
276 model (Fig. 2k), which clearly does not follow a normal distribution with most of the mass concentrated in the

277 lower bounds. In contrast, Q_{50} was not only poorly constrained (Fig. 2g) but was also the upper edge-hitting
278 parameter in the SW model. Moreover, the corresponding distributions of the same parameter in different
279 models were slightly different. For example, the mean of g_{max} in the PM model (0.04 mm s^{-1}) was less than that
280 in the SW model (0.01 mm s^{-1}) (Fig. 2a and 2f, Table 2), except that D_{50} in the PM and SW models and β_2 in the
281 PT-FC and AA models exhibited similar regions. It is interesting to observe that the distribution of K_a in PM
282 model (Figure 2e) has a truncated distribution with highest probability mass at the upper bound, whereas the
283 distribution of K_a in the SW model (Figure 2j) tends to become approximately normal. Overall, the marginal
284 posterior probability density function of most of the individual parameters occupied only a relatively small
285 region compared with the uniform prior distributions, and exhibited relatively large uncertainty reduction.

286 3.2 Performance of the models

287 The performance of each of the four ET models was evaluated over the course of the whole season in 2014.
288 The calibrated parameters of the four models were used and individual ET models were run to estimate the
289 half-hourly λET values. Table 3 summarizes the statistical results for the performance of the models using
290 regression line slope, R^2 , RMSE, MBE, IA, and EF. The regressions between measured and modeled λET values
291 and MBE are shown in Figures 3 and 4, respectively.

292 In general, the four models produced slightly better fits to the measured λET for all the seasons with R^2
293 larger than 0.75 (Fig. 3). However, obvious discrepancies in the predictions made by the models were detected
294 by comparing measured and modeled λET . According to the regression line slope and MBE, the PM model
295 overestimated ET by 1% with a MBE of -9.52 W m^{-2} , and the SW model overestimated ET by 5% with a
296 relatively higher MBE of -19.07 W m^{-2} compared to the PM model. The PT-FC and AA models tended to
297 underestimate λET by 9% and 8% with an MBE of 25.42 and 23.29 W m^{-2} , respectively. From a comparison
298 between the slope and MBE, the PM model performance was higher than that of the other three models, with a
299 slope almost equal to 1 and relatively lower MBE. The SW model was ranked second, while performance of the
300 AA model was slightly higher comparable to that of the PT-FC model. However, if R^2 , RMSE, IA, and EF were
301 used to evaluate performance, the SW model had the best overall performance with $R^2=0.83$, RMSE= 76.34 W
302 m^{-2} , IA = 0.95 and EF = 0.79. The second-best model was the PM model, and the PT-FC was ranked third, while
303 the AA model ranked fourth. Based on the analysis of these traditional error metrics, the PT-FC and AA models
304 yielded similar results. The observed and modeled λET for the four ET models were tightly grouped along the

305 regression lines (Figure 3), and the PT-FC and AA models had similar modeled ET values with a similar degree
306 of point scattering along the regression lines (Figure 3c-3d).

307 Figure 4 shows that large seasonal variations arise in MBE for the four ET models. From the variations in
308 MBE, the estimated λ ET values for all models were generally lower than the measured values before the early
309 jointing stage of maize growth (DOY 154-177, left dashed line) and after the late maturity stage (DOY 256-265,
310 right dash line) with the corresponding LAI $< 2.5 \text{ m}^2 \text{ m}^{-2}$. More positive MBE values for the PT-FC and AA
311 models after the late maturity stage indicate their underestimated performances; however, these estimations
312 appeared even more consistent with a symmetrical scattering of points along the 0-0 line (Figure 4c, 4d) during
313 DOY 177-256 with LAI $> 2.5 \text{ m}^2 \text{ m}^{-2}$.

314 3.3 Comparison of the models using BME

315 Since there is currently no theoretical method for selecting power posterior β values, we determined these
316 values using empirical but straightforward methods. For any power coefficient of $\beta \in [0, 1]$, a sample was
317 drawn from the distribution p_β (Eq. 25) through running DREAM. Although adding more β_k values might
318 improve the BME estimation, this was not done because of the computational cost. For each β_k value, at least
319 150,000 DREAM simulations were large enough to ensure convergence. Figure 5 shows the evolution of \ln
320 $p(D|\theta, M)$ for the four models as a function of β for a dataset covering the entire period. The BME for the SW
321 model was substantially larger than that for the other three models, and the BME for the AA model was the
322 smallest. The BME-based model ranking (from the best to the worst) is SW, PM, PT-FC, and AA. The PT-FC
323 and AA models, which consisting the same number of parameters, had similar potential patterns of evolution
324 with respect to the coefficient β_k . The results illustrate that with the addition of parameters, the model
325 complexity and the model performance are both increased.

326 4. Discussion

327 4.1 Parameter uncertainty analysis

328 With regard to the efficiency of the DREAM algorithm, the acceptance rates of the PM (15.3%) and SW
329 (18.9%) models were much higher than those obtained by some Markov Chain Monte Carlo (MCMC) algorithms
330 that have been used in previous studies. (Sadegh et al., 2014). The posterior parameter bounds exhibit a larger

331 reduction using the DREAM algorithm compared with other studies using the Metropolis–Hasting algorithm.
332 This demonstrates that DREAM could efficiently handle problems involving high-dimensionality, multimodality,
333 nonlinearity.

334 The results showed that the assumed prior uncertainty ranges from most parameters in the four models
335 were significantly reduced. This indicates that the observed ET data contained sufficient information to estimate
336 these parameters. Surface conductance g_s and modeled ET in the PM model are relatively insensitive to Q_{50} , D_{50}
337 and K_q . Hence, these parameters could not be well constrained, and further relaxing the ranges for these
338 parameters could not result in physically realistic behavior of the model. The calculation of g_s^c in the SW model
339 is the same as in the PM model, and thus, g_s^c and modeled ET in the SW model are also insensitive to
340 parameters of Q_{50} , D_{50} , K_q . Therefore, these three parameters were also not well constrained in the SW model. In
341 addition, the uncertainties present in the edge-hitting parameters, may be the outcome of model biases or
342 EC-measured ET data errors, or the characteristic time scale of parameters governing the processes affecting ET
343 is not exactly on the order of half-hours (Braswell et al., 2005). For example, Q_{50} and D_{50} govern changes in
344 visible radiation flux and the humidity deficit at which stomatal conductance is half its maximum value,
345 respectively, and these parameters may change over a shorter or longer time scale than half-hours.

346 The ecophysiological parameter g_{max} is a variable in the g_s^c equation in both the PM and SW models, but
347 this parameter is sensitive to g_s^c and has a significant impact on the evaluated ET. Its effects is relatively
348 independent compared to the other meteorological parameters in the models, and therefore this parameter was
349 well specified in the PM and SW models. The posterior mean value of g_{max} (0.04 m s^{-1}) in the PM model from
350 our study was close to that (0.05 m s^{-1}) reported in northwestern China (Li et al., 2013; Zhu et al., 2014), but
351 g_{max} (0.01 m s^{-1}) in the SW model was less than the reported value. Parameter β_l was well constrained in the
352 PT-FC and AA models because it was relatively independent and did not directly relate to other observed
353 variables.

354 Parameter K_a implicitly appears in the surface conductance equation (Eq.2) in PM model and K_a is
355 insensitive to g_s and modeled ET (Leuning et al., 2008). In contrast, K_a is contained in the equation of net
356 radiation flux into the substrate (Eq.10) in the SW model. This parameter can explicitly partition the total
357 available energy into that absorbed by the canopy and by the soil in the SW model. An analysis of equation (10),

358 found that the variation of K_a could not only account for the extinction effect but also correct the energy forcing
359 data errors. This also meant that the estimated value of K_a using calibration data was actually not just the true
360 extinction coefficient, but also included the energy imbalance correction in the SW model. From this analysis,
361 we could see that K_a not only involved the distribution of energy between the canopy and the soil surface but
362 also the energy imbalance. Therefore, parameter K_a has a great influence on the performance of the SW model.
363 This is why K_a is poorly constrained in the PM model but well constrained in the SW model. To further illustrate
364 the insights regarding the influence of parameter K_a on the performance of the SW model, we calibrated the SW
365 model again and reran the model with a constant value of K_a . The results showed a significant reduction in
366 model performance when K_a was held constant. This implied that the main reason for the SW model
367 outperforming the PM model in our study was not only the more physically rigorous structure of the SW model
368 but also the key parameter K_a being well constrained in the SW model.

369 In general, parameters related to soil surface resistance in the SW model were well evaluated, while
370 parameters related to canopy surface resistance in PM and SW models were poorly estimated. Therefore, using a
371 reliable canopy surface resistance equation in the ET model was crucial for improving its performance. In
372 addition, in our study, the traditional approach was used to quantify the uncertainty, which assumed that the
373 uncertainty mainly arose because of the parameter uncertainty. However, this method cannot explicitly consider
374 errors in the input data and model structural inadequacies. This is unrealistic for real applications, and it is
375 desirable to develop a more reliable inference method to treat all sources of uncertainty separately and
376 appropriately (Vrugt et al., 2008). Moreover, simultaneous direct measurement by micro-lysimeter of sap flow
377 and daily soil evaporation will further help to constrain the model parameters.

378 **4.2 Evaluation and selection of the models**

379 In this study, the traditional statistical measures and BME were chosen to evaluate and compare the
380 performance of four ET models. From the respective composition of these measures, the statistical measures can
381 be divided into residual-based metrics (such as regression slope and MBE) and squared-residual-based measures
382 (such as R^2 , RMSE, IA, and EF). The rankings of the models obtained using the same type of metric
383 (residual-based or squared-residual-based) are similar. Slope and MBE, for example, which are both
384 residual-based measures, produce identical rankings. However, the rankings produced by metrics of different
385 types are not the same. For example, the PM model outperforms the SW model according to the residual-based

386 metrics, but the performance of the PM model is worse than SW model based on the squared-residual-based
387 measures. The comparative analysis shows a consistency between BME and the squared-residual-based metrics
388 (hence the residual-based metrics disagreed with the BME measures). This reveals that the more complex SW
389 model is the best model based on BME and squared-residual-based statistics. The rank order of overall
390 performance of the models from best to worst is: SW, PM, PT-FC, and AA model.

391 Previous studies had shown that BME evaluated by TI provided estimates similar to the true values, and
392 selected the true model if the true model was included within the candidate models (Marshall et al., 2005;
393 Lartillot and Philippe, 2006). Meanwhile, some have argued that Bayesian analysis would choose the simplest
394 model (Jefferys and Berger, 1992; Xie et al., 2011) because of the best trade-off between good fit with the data
395 and model complexity (Schöniger et al., 2014). In this case, the most complex SW model had the highest BME
396 and was chosen as the model with the best performance. This probably resulted from the fact that the complex
397 SW model is indeed the most reliable model among the alternative ET models and can provide a good fit to
398 justify its higher complexity. The SW model is a two-layer model, and simulates soil evaporation and plant
399 transpiration separately, whereas the PM model is a single-layer model in which the plant transpiration and soil
400 evaporation cannot be separated (Monteith, 1965). The PT-FC model is a simplified version of the PM model,
401 and only requires meteorological and radiation information (Priestley and Taylor, 1972), whereas the AA model
402 only relies on the feedback between actual ET and potential ET (Brutsaert and Stricker, 1979). Based on these
403 physical mechanisms and processes that each of these ET models take into account, the rank order of the models
404 is reasonable.

405 The results indicate that the SW model is the best performing model in terms of squared-residual-based
406 metrics, which results from the ability of the model to fit the measured data, irrespective of model complexity. It
407 was interesting to note that both the squared-residual-based measures and the BME consistently yielded the
408 same rank order. Although the squared-residual-based metrics seemed to identify a reasonable rank order, this
409 has not been the case, since the simple traditional statistical measures were known to usually provide a biased
410 view of the efficacy of a model (Kessler and Neas, 1994; Legates and McCabe, 1999). In addition, sensitivity to
411 outliers is associated with these metrics and leads to relatively high values due to the squaring of the residual
412 terms (Willmott, 1981). Furthermore, these traditional statistical metrics ignores the priors, without penalizing
413 model complexity, which is in fact used in a Bayesian analysis. PT-FC and AA, provide identical estimates of

414 R^2 and IA. This is most likely because both models had the same dimension and a similar model structure.
415 Marshall et al. (2005) argued that EF would provide an incorrect conclusion, and Samani et al. (2018) suggested
416 that RMSE would select the complex model as the best performing model. As for slope and MBE, the rankings
417 produced by these residual-based metrics were in obvious disagreement with the one based on BME. Part of the
418 lower values of slope and MBE may be counter-balanced by the higher values of slope and MBE, thus these
419 criteria provide an erroneous and unreliable evaluation of the models. Therefore, the squared-residual-based and
420 residual-based measures were not certain to provide reasonable results in terms of model ranking.

421 BME is a consistent model selection which tries to identify which of the models produced the observed
422 data. Conversely, nonconsistent model selection uses the available data to estimate which of the models might
423 be best in predicting the future data. In fact, the error metrics are essentially nonparsimonious model selection,
424 which is a special case of nonconsistent model selection, where only the goodness of fit is used for rating
425 models without penalizing the model complexity and thus lacking consistency for the selected model (Höge et
426 al., 2018). The consistency between BME and the squared-residual-based metrics only indicates that the optimal
427 model evaluated by BME would also provide the best predictions, and thus consistent model selection should
428 also be asymptotically efficient (Leeb & Pötscher, 2009; Shao, 1997).

429 **4.3 Analysis of model-data mismatch**

430 Conceptual and structural inadequacies of the hydrological model together with measurement errors of the
431 model input (forcing) and output (calibration) data introduce errors in the estimated parameters and model
432 simulations (Laloy, 2015). Hydrological systems are indeed heavily input-driven and errors in forcing data can
433 dramatically impair the quality of calibration results and model output (Bardossy and Das, 2008; Giudice, 2015).
434 Measurement errors occur for a variety of reasons, including unreasonable gap-filling in rainy days; dew and fog;
435 inadequate areal coverage of point-scale soil water measurement; mechanical limitations of the EC system; and
436 inaccurate measurements of wind-speed, soil water, radiation and vapor pressure deficit. ET processes is
437 described using equations that can only capture parts of the complex natural processes and any ET model is an
438 inherent simplification of the real system. These inadequacies can thus lead to biased parameters and
439 implausible predictions.

440 In our study, the results indicated that the PM and SW models overestimated the half-hourly ET compared

441 to the measured ET. Several studies also indicated that ET was overestimated by the PM model (Fisher et al.,
442 2005; Ortega-Farias et al., 2006; Li et al., 2015) and the SW model (Li et al., 2013; Li et al., 2015; Zhang et al.,
443 2008). Possible reasons for the inaccurate estimates included the following: (1) Anisotropic turbulence with
444 weak vertical and strong horizontal fluctuation leads to energy imbalance. The total turbulent heat flux was
445 lower by ~10–30% compared to the available energy in many land surface experiments (Tsvang et al., 1991;
446 Beyrich et al., 2002; Oncley et al., 2007; Foken et al., 2010) and influx networks (Franssen et al., 2010). Liang
447 et al. (2017) also showed an energy imbalance result in the semiarid area in China, and indicated that the energy
448 balance closure ratio ranged from 0.52 to 0.90 during the day, whereas it was about 0.25 at night. However, the
449 measured ET only included vertical flux and not horizontal flux, leading to the measured ET being lower than
450 that of ET predicted by the PM and SW models using the available energy. (2) The absence of a mechanistic
451 representation of the physiological response to plant hydrodynamics makes it difficult for the available ET
452 models to resolve the dynamics of intradaily hysteresis, producing patterns of diurnal error, while the imbalance
453 or lack of between-leaf water demand and soil water supply imposes hydrodynamic limitations on stomatal
454 conductance (Thomsen et al., 2013; Zhang et al., 2014; Matheny et al., 2014). Li et al. (2015) also concluded
455 that neglecting the restrictive effect of the soil on water transport in empirical canopy resistance equations can
456 result in large errors in the partial canopy stage. However, these equations can estimate ET accurately under the
457 full canopy stage (Alves and Pereira, 2000; Katerji and Rana, 2006; Katerji et al., 2011; Rana et al., 2011). Li et
458 al. (2015) showed that the PM model combined with canopy resistance overestimated maize ET during the
459 partial and dense canopy stages by 16% and 13%, respectively. Moreover, in a study of ET in vineyards,
460 Leuning (2008) found that the PM model coupled with canopy resistance overestimated ET during the entire
461 growth stage by 29%.

462 The estimates for ET produced by the PT-FC and AA models were generally lower than the measured
463 values during the entire season. In addition, the four models also underestimated ET during periods of partial
464 cover ($LAI < 2.5 \text{ m}^2 \text{ m}^{-2}$). The PT-FC and AA models consistently underestimated ET, especially during the late
465 maturity stage. The underestimation probably resulted from the following: (1) Non classical situations, such as
466 the oasis effect, may occur in the study area. Strong evaporation from the moist ground and plants results in
467 latent heat cooling. However, this upward latent heat flux was opposed by a downward sensible heat flux from
468 the warm air to the cool ground, and thus the latent heat flux was positive while the sensible heat flux is
469 negative. Therefore, the latent heat flux can be greater in magnitude than the solar heating, because of the

470 additional energy extracted from the warm air by evaporation (Stull, 1988). (2) The lack of mechanistic
471 representation of rainfall interception in ET models probably led to inaccurate simulation for periods soon after
472 rainy days. Bohn and Vivoni (2016) found that evaporation of canopy interception accounted for 8% of the
473 annual ET across the North American monsoon region. Comparing the AA and PT-FC models, the former
474 includes forcing data of available radiation, soil water content and relative humidity, but the PT-FC model only
475 requires available radiation and soil water content and is independent of relative humidity. However, the similar
476 statistical results and similar degrees of MBE scatter indicate that relative humidity has little influence on the
477 AA model simulation. The consistent and consecutive underestimation of ET by the PT-FC and AA models
478 during the late maturity stage show that the model-data disagreement is not caused by regional advection and
479 rainfall interception, because atmospheric processes and thermally-induced circulation can only occur at certain
480 times and during certain days. Therefore, we think that the consistent underestimation of ET by the PT-FC and
481 AA models results primarily from conceptual and structural inadequacies, energy imbalance, and soil water
482 stress. Although the PM and SW models share a common theoretical basis and the PT-FC model is a
483 simplification of the PM model, these models perform significantly differently. Part of the overestimation of ET
484 by the PM and SW models, caused by coupling with the canopy resistance, may be offset by underestimation
485 caused by energy imbalance and soil water stress. However, underestimation of ET by the PT-FC and AA
486 models cannot be counterbalanced by overestimation during the later maturity stage because the PT-FC and AA
487 models are independent of the canopy resistance. Consequently, the half-hourly patterns of errors in the
488 estimates of ET by the PM and SW models are characterized by symmetry and a low degree of scatter, but the
489 PT-FC and AA models exhibit consistently asymmetrical error patterns. By contrast, other studies showed that
490 the PM model (Kato et al., 2004) and the SW model (Chen et al., 2015) underestimated half-hourly ET. As for
491 the PT-FC and AA models, some studies reported that the PT-JPL (Zhang et al., 2017) and the AA model
492 showed an overall poor performance (Zhang et al., 2017). While other studies have indicated that the AA
493 method performed well for both maize and canola crops (Liu et al., 2012). Therefore, the performance of the
494 four ET models appears to vary not only for different crops and locations but also for different meteorological,
495 physiological and soil conditions. Moreover, the performance is also related to the stage of crop growth. Note
496 that these conclusions about the ET models evaluation are derived from traditional error metrics rather than
497 those based on BME model selection. It would be desirable to use available data from other study areas or from
498 other crops for BME-based model selection to confirm whether the SW model is the optimal model under other

499 conditions. Overall, combined with the parameter uncertainty analysis described in Section 4.1, we conclude that
500 energy imbalance and energy interaction between canopy and soil surface have a greater impact on the model
501 performance. And thus, explicitly treating of energy error, and incorporating the elements of existing hydrologic
502 theory about energy interaction between canopy and surface or conceptually correcting the energy interaction
503 are a practicable option for model improvement and application.

504 **5. Conclusions**

505 This study illustrated the application of the Bayesian approach on the statistical analysis and model
506 selection of four widely used ET models. The results showed that the DREAM algorithm successfully reduced
507 the assumed prior uncertainties for most of the parameters in the four models. In the model calibration, the key
508 parameters which had a significant influence on ET simulations were well constrained. The main reasons for the
509 outperforming of SW model were its physically rigorous structure and the extinction coefficient parameter,
510 which is sensitive and has a significant impact on the performance of the model, being well constrained. BME is
511 a consistent model selection to identify the best fitting to the observed data. Although the squared-residual-based
512 metrics, including R^2 , IA, RMSE, and EF, produced a ranking identical to that of BME, it must be noted that
513 these squared-residual-based metrics do not allow using prior information and do not penalize the model
514 complexity when comparing the models. Therefore, some cautions are needed when using these statistical
515 methods to compare different models.

516 The model–data discrepancies were analyzed to facilitate model improvement after Bayesian model
517 calibration and comparison. The results indicate that the discrepancies arose mainly as a result of energy
518 imbalance caused by anisotropic turbulence, additional energy induced by advection processes, the absence of a
519 mechanistic representation of the physiological response to plant hydrodynamics and the energy interaction
520 between canopy and surface. Among these causes, energy imbalance and additional energy are related to forcing
521 data errors rather than to an unreasonable model structure. Thus, understanding the process of the physiological
522 response to plant hydrodynamics and the interaction between canopy and surface is essential for improving the
523 performance of evapotranspiration models. Overall, the applications of Bayesian calibration, Bayesian model
524 evaluation and analysis of model–data discrepancies in our study, provide a promising framework for reducing
525 uncertainty and improving the performance of ET models. It would be desirable to confirm whether the SW is
526 the optimal model using data of other crops or other climate regions.

527 **Author contribution**

528 Guoxiao Wei and Xiaoying Zhang designed the experiments. Ning Yue and Fei Kan carried them out.
529 Ming Ye developed the model selection scheme. Guoxiao Wei performed the simulations. Guoxiao Wei and
530 Xiaoying Zhang prepared the manuscript with contributions from all co-authors.

531 **Competing interests**

532 The authors declare that they have no conflict of interest.

533 **Acknowledgments**

534 We thank Ying Guo, Huihui Dang, Jun Dong for the data collection and analysis. This work was funded by
535 the National Natural Science Foundation of China Nos. 41471023 and Nos.41702244. The third author was
536 supported in part by DOE Early Career Award DE-SC0008272 and National Science Foundation-Division of
537 Earth Science Grant 1552329. All observed data used in this study are from Heihe Watershed Allied Telemetry
538 Experimental Research (HiWATER). We thank all the staff who participated in HiWATER field campaigns.
539 Considerate and helpful comments by anonymous reviewers have considerably improved the manuscript.

540 **References**

- 541 Allen, R. G., Perista, L. S., Raes, D., and Smith, M.: Crop Evapotranspiration-Guidelines for Computing Crop
542 Water Requirements; FAO Irrigation and Drainage apers-56, FAO-Food and Agriculture Organization
543 of the United Nations, Rome, 1998.
- 544 Alves, I. and Pereira, L. S.: Modeling surface resistance from climatic variables? Agric. Water Manage., 42,
545 371–385, 2000.
- 546 Aubinet, M., Grelle, A., Ibrom, A., Rannik, Ü., Moncrieff, J., and Foken, T.: Estimates of the annual net carbon
547 and water exchange of forests: the euroflux methodology, Adv. Ecol. Res., 30(1), 113-175, 2000.
- 548 Baldocchi, D. D.: Assessing the eddy covariance technique for evaluating carbon dioxide exchange rates of
549 ecosystems: past, present and future, Glob. Change. Biol., 9, 479–492, 2003.
- 550 Bardossy, A., and Das, T.: Influence of rainfall observation network on model calibration and application,
551 Hydrol. Earth Syst. Sci., 12(1), 77-89, doi:10.5194/hess-12-77-2008, 2008.
- 552 Barton. I. J.: A Parameterization of the Evaporation from Nonsaturated Surfaces, J. Appl Meteorol., 18(1), 43-47,
553 1979.
- 554 Beyrich, F., Richter, S. H., Weisensee, U., Kohsiek, W., Lohse, H., de Bruin, H. A. R., Foken, T., Göckede, M.,
555 Berger, F., Vogt, R., and Batchvarova, E.: Experimental determination of turbulent fluxes over the
556 heterogeneous litfass area: selected results from the litfass-98 experiment, Theor. Appl. Climatol.,
557 73(1–2), 19–34, doi:10.1007/s00704-002-0691-7, 2002.
- 558 Bohn, T. J., and Vivoni, E. R.: Process-based characterization of evapotranspiration sources over the North
559 American monsoon region, Water Resour. Res., 52, 358–384, doi:10.1002/2015WR017934, 2016.
- 560 Bonan, G.: Ecological climatology: concepts and applications, Cambridge University Press, 2008.
- 561 Braswell, B. H., Sacks, W. J., Linder, E., and Schimel, D. S.: Estimating diurnal to annual ecosystem parameters
562 by synthesis of a carbon flux model with eddy covariance net ecosystem exchange observations, Global
563 Change. Biol., 11, 335–355, 2005,
- 564 Brutsaert, W., and Han, S.: An advection-aridity approach to estimate actual regional evapotranspiration, Water

- 565 Resour. Res., 15(2), 443-450, 1979.
- 566 Brutsaert, W.: Hydrology: An Introduction. Cambridge University Press, Cambridge, 2005.
- 567 Chen, D. Y., Wang, X., Liu, S. Y., Wang, Y. K., Gao, Z. Y., Zhang, L. L., Wei, X. G., and Wei, X. D.: Using
568 Bayesian analysis to compare the performance of three evapotranspiration models for rainfed jujube
569 (*Ziziphus jujuba* Mill.) plantations in the Loess Plateau, *Agr. Water Manage.*, 159, 341–357, 2015.
- 570 Elshall, A. S., Ye, M., Pei, Y., Zhang, F., Niu, G. Y., and Barron-Gafford, G. A.: Relative model score: A scoring
571 rule for evaluating ensemble simulations with application to microbial soil respiration modeling, *Stoch.*
572 *Env. Res. A.*, 1-11, DOI: 10.1007/s00477-018-1592-3, 2018.
- 573 Ershadi, A., McCabe, M. F., Evans, J. P., Chaney, N. W., and Wood, E. F.: Multi-site evaluation of terrestrial
574 evaporation models using fluxnet data, *Agric. For. Meteorol.*, 187(8), 46-61, 2014.
- 575 Ershadi, A., McCabe, M. F., Evans, J. P., and Wood, E. F.: Impact of model structure and parameterization on
576 Penman–Monteith type evaporation models, *J. Hydrol.*, 525, 521–535, 2015.
- 577 Fisher, J. B., DeBiase, T. A., Qi, Y., Xu, M., and Goldstein, A. H.: Evapotranspiration models compared on a
578 Sierra Nevada forest ecosystem, *Environ. Model. Softw.*, 20 (6), 783–796, 2005.
- 579 Flint A. L., Childs, S. W.: Use of the Priestley–Taylor evaporation equation for soil water limited conditions in a
580 small forest clearcut, *Agric. For. Meteorol.*, 56(3–4), 247–260, 1991.
- 581 Foken, T., Mauder, M., Liebethal, C., Wimmer, F., Beyrich, F., Leps, J. P., Raasch, S., DeBruin, H. A. R.,
582 Meijninger, W. M. L., and Bange, J.: Energy balance closure for the LITFASS-2003 experiment, *Theor.*
583 *Appl. Climatol.*, 101(1–2), 149–160, doi:10.1007/s00704-009-0216-8, 2010.
- 584 Franssen, H. J. H., Stöckli, R., Lehner, I., Rotenberg, E., and Seneviratne S. I.: Energy balance closure of
585 eddy-covariance data: A multisite analysis for European FLUXNET stations, *Agric. For. Meteorol.*,
586 150(12), 1553–1567, doi:10.1016/j.agrformet.2010.08.005, 2010.
- 587 Gelman, A., and Rubin, D. B.: Inference from iterative simulation using multiple sequences, *Stat. Sci.*, 7, 457–
588 472, 1992.
- 589 Gelman, A.: Simulating normalizing constants: From importance sampling to bridge sampling to path sampling,
590 *Stat. Sci.* 13, 163–185, 1998.
- 591 Giudice, D., Albert, C., Rieckermann, J., and Reichert, P.: Describing the catchment-averaged precipitation as a
592 stochastic process improves parameter and input estimation, *Water Resour. Res.*, 52, 3162–3186,
593 doi:10.1002/2015WR017871, 2016.
- 594 Höge, M., Wöhling, T., and Nowak, W.: A primer for model selection: The decisive role of model complexity.
595 *Water Resour. Res.*, 54, 1688–1715, doi.org/10.1002/2017WR021902, 2018.
- 596 Jefferys, W. H., and Berger, J. O.: Sharpening Ockham’s razor on a Bayesian strop, *Am. Sci.*, 89, 64-72, 1992.
- 597 Kashyap, R. L.: Optimal choice of AR and MA parts in autoregressive moving average models, *IEEE Trans.*
598 *Pattern Anal. Mach. Intell.*, 4(2), 99–104, 1982.
- 599 Katerji, N., and Rana, G.: Modelling evapotranspiration of six irrigated crops under Mediterranean climate
600 conditions, *Agric. For. Meteorol.*, 138, 142–155, 2006.
- 601 Katerji, N., Rana, G., Fahed, S.: Parameterizing canopy resistance using mechanistic and semi-empirical
602 estimates of hourly evapotranspiration: critical evaluation for irrigated crops in the Mediterranean,
603 *Hydrol. Process.*, 25, 117–129, 2011.
- 604 Kato, T., Kimura, R., and Kamichika, M.: Estimation of evapotranspiration, transpiration ratio and water-use
605 efficiency from a sparse canopy using a compartment model, *Agric. Water Manage.*, 65, 173–191,
606 2004.
- 607 Kessler, E., and Neas, B.: On correlation, with applications to the radar and raingage measurement of rainfall,
608 *Atmos. Res.*, 34, 217-229, 1994.
- 609 Laloy, E., Linde, N., Jacques, D., and Vrugt, J. A.: Probabilistic inference of multi-Gaussian fields from indirect
610 hydrological data using circulant embedding and dimensionality reduction, *Water Resour. Res.*, 51,
611 4224–4243, doi:10.1002/2014WR016395, 2015.
- 612 Lartillot, N., and Philippe, H.: Computing Bayes factors using thermodynamic integration, *Syst. Biol.*, 55(2),
613 195-207, 2006.
- 614 Leeb, H., and Pötscher, B. M.: Model selection, Berlin, Germany: Springer., pp, 889–925,
615 doi.org/10.1007/978-3-540-71297-839, 2009.
- 616 Legates, D. R., and McCabe, G. J.: Evaluating the use of “goodness-of-fit” measures in hydrologic and
617 hydroclimatic model validation, *Water Resour. Res.*, 35, 233–241, 1999.
- 618 Leuning, R., Zhang, Y. Q., Rajaud, A., Cleugh, H., and Tu, K.: A simple surface conductance model to estimate
619 regional evaporation using MODIS leaf area index and the Penman–Monteith equation, *Water Resour.*

- 620 Res., 44, W10419, doi.org/10.1029/2007WR006562, 2008.
- 621 Liang, J., Zhang, L., Cao, X., Wen, J., Wang, J., and Wang, G.: Energy balance in the semiarid area of the Loess
622 Plateau, China, *J. Geophys. Res. Atmos.*, 122, 2155–2168, doi:10.1002/2015JD024572, 2017.
- 623 Li, S., Kang, S., Zhang, L., Ortega-Farias, S., Li, F., Du, T., Tong, L., Wang, S., Ingman, M., and Guo, W.:
624 Measuring and modeling maize evapotranspiration under plastic film-mulching condition, *J. Hydrol.*,
625 503, 153–168, 2013.
- 626 Li, S., Zhang, L., Kang, S., Tong, L., Du, T., Hao, X., Zhao, P.: Comparison of several surface resistance models
627 for estimating crop evapotranspiration over the entire growing season in arid regions. *Agric. For.*
628 *Meteorol.* 208, 1-15, 2015.
- 629 Li, X., Cheng, G. D., Liu, S. M., Xiao, Q., Ma, M. G., Jin, R., Che, T., Liu, Q. H., Wang, W. Z., Qi, Y., Wen, J.
630 G., Li, H. Y., Zhu, G. F., Guo, J. W., Ran, Y. H., Wang, S. G., Zhu, Z. L., Zhou, J., Hu, X. L., and Xu, Z.
631 W.: Heihe Watershed Allied Telemetry Experimental Research (HiWATER): Scientific objectives and
632 experimental design, *B. Am. Meteorol. Soc.*, 94, 1145–1160, 2013.
- 633 Liu, S. M., Xu, Z. W., Wang, W. Z., Jia, Z. Z., Zhu, M. J., Bai, J., and Wang, J. M.: A comparison of
634 eddy-covariance and large aperture scintillometer measurements with respect to the energy
635 balance closure problem, *Hydrol. Earth Syst. Sci.*, 15, 1291–1306, doi:10.5194/hess-15-1291-2011,
636 2011.
- 637 Liu, G., Liu, Y., Hafeez, M., Xu, D., Vote, C.: Comparison of two methods to derive time series of actual
638 evapotranspiration using eddy covariance measurements in the southeastern Australia, *J. Hydrol.*, 454–
639 455 (4), 1–6, 2012.
- 640 Liu, P., Elshall, A. S., Ye, M., Beerli, P., Zeng, X., Lu, D., and Tao, Y.: Evaluating marginal likelihood with
641 thermodynamic integration method and comparison with several other numerical methods. *Water*
642 *Resour. Res.*, 52(2), 734-758, doi:10.1002/2014WR016718, 2016.
- 643 Marshall, L., Nott, D., and Sharma, A.: Hydrological model selection: A Bayesian alternative, *Water Resour.*
644 *Res.*, 41(10), 3092-3100, doi: 10.1029/2004WR003719, 2005.
- 645 Matheny, A. M., Bohrer, G., Stoy, P. C., Baker, I. T., Black, A. T., Desai, A. R., Dietze, M. C., Gough, C. M.,
646 Ivanov, V. Y., Jassal, R. S., Novick, K. A., Schäfer, K. V. R., and Verbeeck, H.: Characterizing the
647 diurnal patterns of errors in the prediction of evapotranspiration by several land-surface models: An
648 NACP analysis, *J. Geophys. Res. Biogeosci.*, 119(7), 1458-1473, 2014.
- 649 Monteith, J. L.: Evaporation and environment, *Symp. Soc. Exp. Biol.*, 19, 205–234, 1965.
- 650 Morison, J. I. L., Baker, N. R., Mullineaux, P. M., and Davies, W. J.: Improving water use in crop production,
651 *Philos. T. Roy. Soc. B.*, 363, 639–658, 2008.
- 652 Neal, R. M.: Markov chain sampling methods for Dirichlet process mixture models, *J. Comput. Graph. Stat.*, 9,
653 249–265, 2000.
- 654 Oncley, S. P., Foken, T., Vogt, R., Kohsiek, W., DeBruin, H., Bernhofer, C., Christen, A., Van Gorsel, E., Grantz,
655 D., and Feigenwinter, C.: The energy balance experiment EBEX-2000. Part I: Overview and energy
656 balance, *Boundary Layer Meteorol.*, 123(1), 1–28, doi:10.1007/s10546-007-9161-1, 2007.
- 657 Ortega-Farias, S., Oliso, A., Fuentes, S., and Valdes, H.: Latent heat flux over a furrow-irrigated tomato crop
658 using Penman–Monteith equation with a variable surface canopy resistance, *Agric. Water Manage.*, 82,
659 421–432, 2006.
- 660 Ortega-Farias, S., Poblete-Echeverria, C., and Brisson, N.: Parameterization of a two-layer model for estimating
661 vineyard evapotranspiration using meteorological measurements, *Agr. For. Meteorol.*, 150, 276–286,
662 2010.
- 663 Parlange, M. B., and Katul, G. G.: An advection-aridity evaporation model, *Water Resour. Res.*, 28 (1), 127-132,
664 1992.
- 665 Poblete-Echeverria, C., and Ortega-Farias, S.: Estimation of actual evapotranspiration for a drip-irrigated Merlot
666 vineyard using a three-source model, *Irrig. Sci.*, 28, 65–78, 2009.
- 667 Priestley, C. H. B., and Taylor, R. J.: On the assessment of surface heat flux and evaporation using large-scale
668 parameters, *Mon. Weather Rev.*, 100 (2), 81-92, 1972.
- 669 Rana, G., Katerji, N., Ferrara, R.M., and Martinelli, N.: An operational model to estimate hourly and daily crop
670 evapotranspiration in hilly terrain: validation on wheat and oat crops, *Theory Appl. Climatol.*, 103,
671 413–426, 2011.
- 672 Sadegh, M., and Vrugt J. A.: Approximate Bayesian Computation using Markov Chain Monte Carlo simulation:
673 DREAM(ABC), *Water Resour. Res.*, 50, 6767–6787, doi:10.1002/2014WR015386, 2014.
- 674 Samani, S., Ye, M., Zhang, F., Pei, Y. Z., Tang, G. P., Elshall, A. S., and Moghaddam, A. A.: Impacts of prior

675 parameter distributions on bayesian evaluation of groundwater model complexity, *Water Science &*
676 *Engineering.*, 11(2), 89-100, doi.org/10.1016/j.wse.2018.06.001, 2018.

677 Schöniger, A., Wohling, T., Samaniego, L., and Nowak, W.: Model selection on solid ground: Rigorous
678 comparison of nine ways to evaluate Bayesian model evidence, *Water Resour. Res.*, 50, 9484–9513,
679 doi:10.1002/2014WR016062, 2014.

680 Schwarz, G.: Estimating the dimension of a model, *Ann. Stat.*, 6(2), 461–464, doi:10.1214/aos/1176344136,
681 1978.

682 Shao, J.: An asymptotic theory for linear model selection, *Statistica Sinica*, 7(2), 221–242, 1997.

683 Shuttleworth, W. J., Gurney, R. J.: The theoretical relationship between foliage temperature and canopy
684 resistance in sparse crops, *Q. J. Roy. Meteorol. Soc.*, 116, 497–519, 1990.

685 Stannard, D. I.: Comparison of Penman-Monteith, Shuttleworth-Wallace, and modified Priestley-Taylor
686 evapotranspiration models for wildland vegetation in semiarid rangeland, *Water Resour. Res.*, 29 (5),
687 1379-1392, 1993.

688 Stull, R. B.: An introduction to boundary layer meteorology, Kluwer Academic Publ., 255pp, 1988.

689 Sumner, D. M., and Jacobs, J. M.: Utility of Penman–Monteith Priestley–Taylor reference evapotranspiration,
690 and pan evaporation methods to estimate pasture evapotranspiration, *J. Hydrol.*, 308 (1-4), 81-104,
691 2005.

692 Szilagyi, J., and Jozsa, J.: New findings about the complementary relationship based evaporation estimation
693 methods, *J. Hydrol.*, 354: 171–186, 2008.

694 Thomsen, J., Bohrer, G., Matheny, M. V., Ivanov, Y., He, L., Renninger, H., and Schäfer, K.: Contrasting
695 hydraulic strategies during dry soil conditions in *Quercus rubra* and *Acer rubrum* in a sandy site in
696 Michigan, *Forests.*, 4(4), 1106–1120, 2013.

697 Tsvang, L., Fedorov, M., Kader, B., Zubkovskii, S., Foken, T., Richter, S., and Zeleny, Y.: Turbulent exchange
698 over a surface with chessboardtype inhomogeneities, *Boundary Layer Meteorol.*, 55(1–2), 141–160,
699 1991.

700 Vinukollu R, K., Wood, E. F., Ferguson, C. R., and Fisher, J. B.: Global estimates of evapotranspiration for
701 climate studies using multi-sensor remote sensing data: evaluation of three process-based approaches,
702 *Remote Sens. Environ.*, 115(3), 801–823, 2011.

703 Vrugt, J. A., ter Braak, C. J. F., Clark, M. P. J., Hyman, M., and Robinson, B. A.: Treatment of input uncertainty
704 in hydrologic modeling: Doing hydrology backward with Markov chain Monte Carlo simulation, *Water*
705 *Resour. Res.*, 44, W00B09, doi:10.1029/2007WR006720, 2008.

706 Vrugt, J. A., ter Braak, C. J. F., Diks, C. G. H., Higdon, D., Robinson, B. A., and Hyman, J. M.: Accelerating
707 Markov chain Monte Carlo simulation by differential evolution with self-adaptive randomized
708 subspace sampling, *Int. J. Nonlinear Sci. Numer. Simul.*, 10(3), 273-290, 2009.

709 Webb, E. K., Pearman, G. I., and Leuning, R.: Correction of flux measurements for density effects due to heat
710 and water-vapor transfer, *Q. J. R. Meteorol. Soc.*, 106(447), 85–100, 1980.

711 Willmott, C. J.: On the validation of models, *Phys. Geogr.*, 2, 184-194, 1981.

712 Xie, W., Lewis, P. O., Fan, Y., Kuo, L., and Chen, M. H.: Improving marginal likelihood estimaton for Bayesian
713 phylogenetic model selection, *Syst. Biol.*, 60(2), 150-160, 2011.

714 Xu, C. Y., and Singh, V. P.: A review on monthly water balance models for water resources investigations, *Water*
715 *Resour. Manage.*, 12, 31-50, 1998.

716 Xu, Z. W., Liu, S. M., Li, X., Shi, S. J., Wang, J. M., Zhu, Z. L., Xu, T. R., Wang, W. Z., and Ma, M. G.:
717 Intercomparison of surface energy flux measurement systems used during the HiWATERUSOEXE, *J.*
718 *Geophys. Res.*, 118, 13140–13157, 2014.

719 Ye, M., Neuman, S. P., and Meyer, P. D.: Maximum likelihood Bayesian averaging of spatial variability models
720 in unsaturated fractured tuff, *Water Resour. Res.*, 40, W05113, doi:10.1029/2003WR002557, 2004.

721 Ye, M., Meyer, P. D., and Neuman, S. P.: On model selection criteria in multimodel analysis, *Water Resour. Res.*,
722 44, W03428, doi:10.1029/2008WR006803, 2008.

723 Zhang, B., Kang, S., Li, F., and Zhang, L.: Comparison of three evapotranspiration models to Bowen
724 ratio-energy balance method for vineyard in an arid desert region of northwest China, *Agr. Forest*
725 *Meteorol.*, 148: 1629–1640, 2008.

726 Zhang, X. Y., Liu, C. X., Hu, B. X., and Zhang, G. N.: Uncertainty analysis of multi-rate kinetics of uranium
727 desorption from sediments, *J. Contam. Hydrol.*, 156(1), 1-15, 2014.

728 Zhang, K., Ma, J., Zhu, G., Ma, T., Han, T., and Feng, L. L.: Parameter sensitivity analysis and optimization for
729 a satellite-based evapotranspiration model across multiple sites using moderate resolution imaging

- 730 spectroradiometer and flux data. *Journal of Geophysical Research: Atmospheres*, 122(1), 230-245,
731 2017.
- 732 Zhu, G. F., Su, Y. H., Li, X., Zhang, K., and Li, C. B.: Estimating actual evapotranspiration from an alpine
733 grassland on Qinghai–Tibetan plateau using a two-source model and parameter uncertainty analysis by
734 Bayesian approach, *J. Hydrol.*, 476, 42–51, 2013.
- 735 Zhu, G. F., Li, X., Su, Y. H., Zhang, K., Bai, Y., Ma, J. Z., Li, C. B., Hu, X. L., and He, J. H.: Simultaneously
736 assimilating multivariate data sets into the two-source evapotranspiration model by Bayesian approach:
737 Application to spring maize in an arid region of northwestern China, *Geosci. Model. Dev.*, 7(4), 1467–
738 1482, 2014.

739 **Appendix A: List of symbols and physical characteristics in ET models**

A	Available energy for the whole canopy (W m^{-2})
A_s	Available energy (W m^{-2})
R_n	Net radiation fluxes into the canopy (W m^{-2})
R_{ns}	Net radiation flux into the substrate (W m^{-2})
G	Soil heat flux (W m^{-2})
λET	Sum of the latent heat flux from the crop (λT) and soil (λE) (W m^{-2})
ET_c	Canopy transpiration (W m^{-2})
ET_s	Soil evaporation (W m^{-2})
C_c	Canopy resistance coefficient (dimensionless)
C_s	Soil surface resistance coefficient (dimensionless)
LAI	Leaf area index
Q_{50}	Visible radiation flux (W m^{-2})
D_{50}	Vapor pressure deficit (kPa)
D_a	Vapor pressure deficit at the reference height ($D_a=e_s-e_a$) (kPa)
Q_h	Flux density of visible radiation at the top of the canopy (W m^{-2})
K_q	Extinction coefficient
K_a	Extinction coefficient
f	Fraction of evaporation soil and total evaporation
λ	Latent heat of water evaporation (MJ kg^{-1})
Δ	Slope of the saturated vapour pressure curve (Pa K^{-1})
γ	Psychrometric constant (kPa K^{-1})
ρ	Density of air (kg m^{-3})
k	Karman constant (0.41)
e_s	Saturated vapor pressure (kPa)
e_a	Actual vapor pressure (kPa)
q^*	Saturation-specific humidity at air temperature (kg kg^{-1})
q	Specific humidity of the atmosphere (kg kg^{-1})
b_1	Empirical constant (s m^{-1})
b_2	Empirical constant (s m^{-1})
β_1	empirical constant
β_2	empirical constant
θ	Soil water content ($\text{m}^3 \text{m}^{-3}$)
θ_a	Critical water content at which plant stress starts ($\text{m}^3 \text{m}^{-3}$)
θ_b	Water content at the wilting point ($\text{m}^3 \text{m}^{-3}$)
θ_r	Residual soil water content ($\text{m}^3 \text{m}^{-3}$)
θ_s	Saturated water content ($\text{m}^3 \text{m}^{-3}$)
Θ	Relative water saturation

d	Zero plane displacement height (m)
z_m	Height of the wind speed and humidity measurements (3 m)
z_{0m}	Roughness length governing the transfer of momentum (m)
z_{0v}	Roughness length governing the transfer of water vapor (m)
h	Canopy height (m)
u_z	Wind speed at height z_m (m s^{-1})
g_a	Aerodynamic conductance (m s^{-1})
g_s	Surface conductance (m s^{-1})
g_{max}	Maximum stomatal conductance of leaves at the top of the canopy (m s^{-1})
g_s^c	Canopy conductance (m s^{-1})
r_a	Aerodynamic resistance (s m^{-1})
r_a^a	Aerodynamic resistance between canopy source height and a reference level (s m^{-1})
r_a^s	Aerodynamic resistance between the substrate and the canopy source height (s m^{-1})
r_a^c	Bulk boundary layer resistance of the vegetation element in the canopy (s m^{-1})
r_s^s	Surface resistance of the canopy (s m^{-1});
r_s^c	Bulk stomatal resistance of the canopy (s m^{-1})

740

741 **Appendix B: Bayesian inference and the DREAM algorithm**

742 The posterior probability distribution of the parameter is calculated by Bayes' theorem:

$$743 \quad \pi(\boldsymbol{\theta} | D, M) \propto \frac{\pi(\boldsymbol{\theta} | M) p(D | \boldsymbol{\theta}, M)}{p(D | M)} \quad (\text{A1})$$

744 where $\pi(\boldsymbol{\theta} | M)$ represents the prior density of $\boldsymbol{\theta}$ under model M ; $p(D | \boldsymbol{\theta}, M)$ is the joint likelihood of
745 model M and its parameters $\boldsymbol{\theta}$; and

$$746 \quad p(D | M) = \int p(D | \boldsymbol{\theta}, M) \pi(\boldsymbol{\theta} | M) d\boldsymbol{\theta} \quad (\text{A2})$$

747 is the marginal likelihood, or Bayesian model evidence (BME).

748 The likelihood function, $p(D | \boldsymbol{\theta}, M)$, used for parameter estimation, is specified according to the

749 distributions of observation errors. Error $e(t)$ in each observation $D(t)$ at time t is expressed by

$$750 \quad e(t) = D(t) - f(t) \quad (\text{A3})$$

751 . Assuming $e(t)$ follows a Gaussian distribution with a zero mean, and the likelihood function can be

752 expressed as

$$753 \quad p(D|\theta) = \prod_{t=1}^n \frac{1}{\sqrt{2\pi}\sigma} e^{-\frac{[e(t)]^2}{2\sigma^2}} \quad (\text{A4})$$

754 where n is the number of observations and σ represents the error variances.

755 In this study, we used the DREAM algorithm (Vrugt et al., 2008, 2009) to explore the ET models'
756 parameter space and to estimate BME. The DREAM sampling scheme is an adaptation of the global
757 optimization algorithm of a shuffled complex evolution metropolis (SCEM-UA). This algorithm was
758 described in more detail in Vrugt et al. (2008, 2009).

759 List of Tables

760 **Table 1.** Prior distributions and parameter limits for the PM, SW, PT-FC and AA models. The values are
761 derived from the literature.

762 **Table 2.** Maximum Likelihood Estimates (MLEs), Mean Estimates, 95% High-Probability Intervals
763 (Lower Limit, Upper Limit).

764 **Table 3.** Slope and coefficient of determination (R^2) of regression between measured and modeled
765 half-hourly evapotranspiration values, and statistics of root mean square error (RMSE), mean bias error
766 (MBE), index of agreement (IA), model efficiency (EF) and Logarithm of BME for the four ET models.

767 List of Figures

768 **Figure 1.** Trace plots of the G-R statistic of Gelman and Rubin (Gelman and Rubin, 1992) using DREAM
769 for the PM model (a) and (b) the SW model. Different parameters are coded with different colors. The
770 dashed line denotes the default threshold used to diagnose convergence to a limiting distribution.

771 **Figure 2.** (a)-(e), (f)-(l), (m)-(n), and (o)-(p) show histograms for the PM (black), SW (cyan), PT-FC
772 (magenta) and AA (orange) models, respectively. These histograms are constructed from all chains for each
773 model and a total of $40,000 \times N$ realizations are simulated using DREAM. The x axes represent the
774 prespecified limits of the parameters.

775 **Figure 3.** Regressions between measured and modeled half-hourly ET values produced by different
776 models from DOY 154 to DOY 270: (a) PM, (b) SW, (c) PT-FC and (d) AA. The regressions are: $Y =$
777 $0.99X$ ($R^2 = 0.76$), $Y = 1.05X$ ($R^2 = 0.82$), $Y = 0.91X$ ($R^2 = 0.75$), and $Y = 0.92X$ ($R^2 = 0.75$) for the PM,
778 SW, PT-FC and AA models, respectively.

779 **Figure 4.** Mean bias error (MBE) of predicted and observed ET values for (a) PM, (b) SW, (c) PT-FC and
780 (d) AA models from DOY 154 to DOY 270. Parameters used for prediction are estimated by DREAM with
781 the dataset for the calibration period from DOY 154 to DOY 202.

782 **Figure 5.** Variation of the mean posterior expectation of the potential y_k with β_k for the PM, SW, PT-FC
783 and AA models.

784

785 **Table 1** Prior distributions and parameter limits for the PM, SW, PT-FC and AA models. The values are
786 derived from the literature.

Parameter	Description	Prior range PM		Prior for SW		Prior for PT and AA		References
		Lower	upper	Lower	upper	Lower	upper	
g_{max} (mm s ⁻¹)	maximum stomatal conductance	0	50	0	50			Kelliher et al. (1995)
Q_{50} (W m ⁻²)	visible radiation flux	10	50	10	50			Leuning et al. (2008)
D_{50} (kPa)	vapor pressure deficit	0.5	3	0.5	3			Leuning et al. (2008)
K_q	extinction coefficient	0	1	0	1			Leuning et al. (2008)
K_a	extinction coefficient	0	1	0	1			Leuning et al. (2008)
b_1 (s m ⁻¹)	empirical constant			4.5	11.3			Sellers et al. (1992)
b_2 (s m ⁻¹)	empirical constant			0	8			Sellers et al. (1992)
β_1	empirical constant					0.5	1.5	Flint et al. (1991);
β_2	empirical constant					0.1	10	Barton. (1979)

787

788 **Table 2** Maximum Likelihood Estimates (MLEs), Mean Estimates, 95% High-Probability Intervals
789 (Lower Limit, Upper Limit).

Parameter	Posterior for PM			Posterior for SW			Posterior for PT and AA		
	MLE	Mean	CI	MLE	Mean	CI	MLE	Mean	CI
g_{max} (mm s ⁻¹)	0.04	0.04	(0.03, 0.04)	0.01	0.01	(0.005, 0.012)			
Q_{50} (W m ⁻²)	49.96	48.52	(39.73, 49.74)	47.49	40.32	(11.02, 48.99)			
D_{50} (kPa)	3.00	2.87	(1.92, 2.97)	2.98	2.88	(2.26, 2.98)			

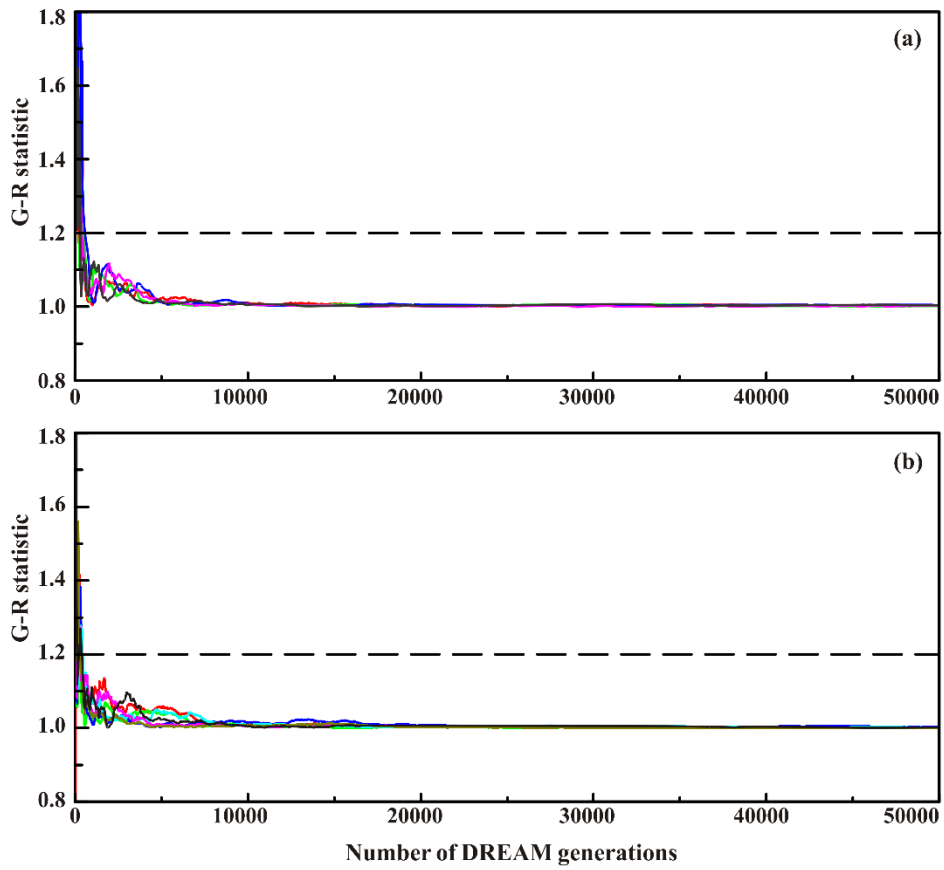
K_q	1.00	0.99	(0.911, 0.998)	0.99	0.88	(0.06, 0.98)		
K_a	1.00	0.98	(0.822, 0.995)	0.12	0.12	(0.074, 0.184)		
b_1 (s m ⁻¹)				4.51	4.57	(4.52, 4.96)		
b_2 (s m ⁻¹)				0.39	0.57	(0.07, 1.38)		
β_1							1.1 ^a	1.098 ^a (1.06, 1.16) ^a
							1.5 ^b	1.499 ^b (1.492, 1.499) ^b
β_2							10.00 ^a	9.75 ^a (7.97, 9.95) ^a
							10.00 ^b	9.94 ^b (9.44, 9.99) ^b

790 ^a PT-FC model; ^b AA model.

791 **Table 3** Slope and coefficient of determination (R^2) of regression between measured and modeled
792 half-hourly evapotranspiration values, and statistics of root mean square error (RMSE), mean bias error
793 (MBE), index of agreement (IA), model efficiency (EF) and Logarithm of BME for the four ET models.

Model	Slope	R^2	RMSE	MBE	IA	EF	BME
PM	1.01	0.76	85.38	-9.52	0.93	0.74	-6300.5
SW	1.05	0.82	76.34	-19.07	0.95	0.79	-6025.1
PT-FC	0.91	0.75	94.39	25.42	0.92	0.68	-6366.8
AA	0.92	0.75	95.09	23.29	0.92	0.67	-6390.3

794

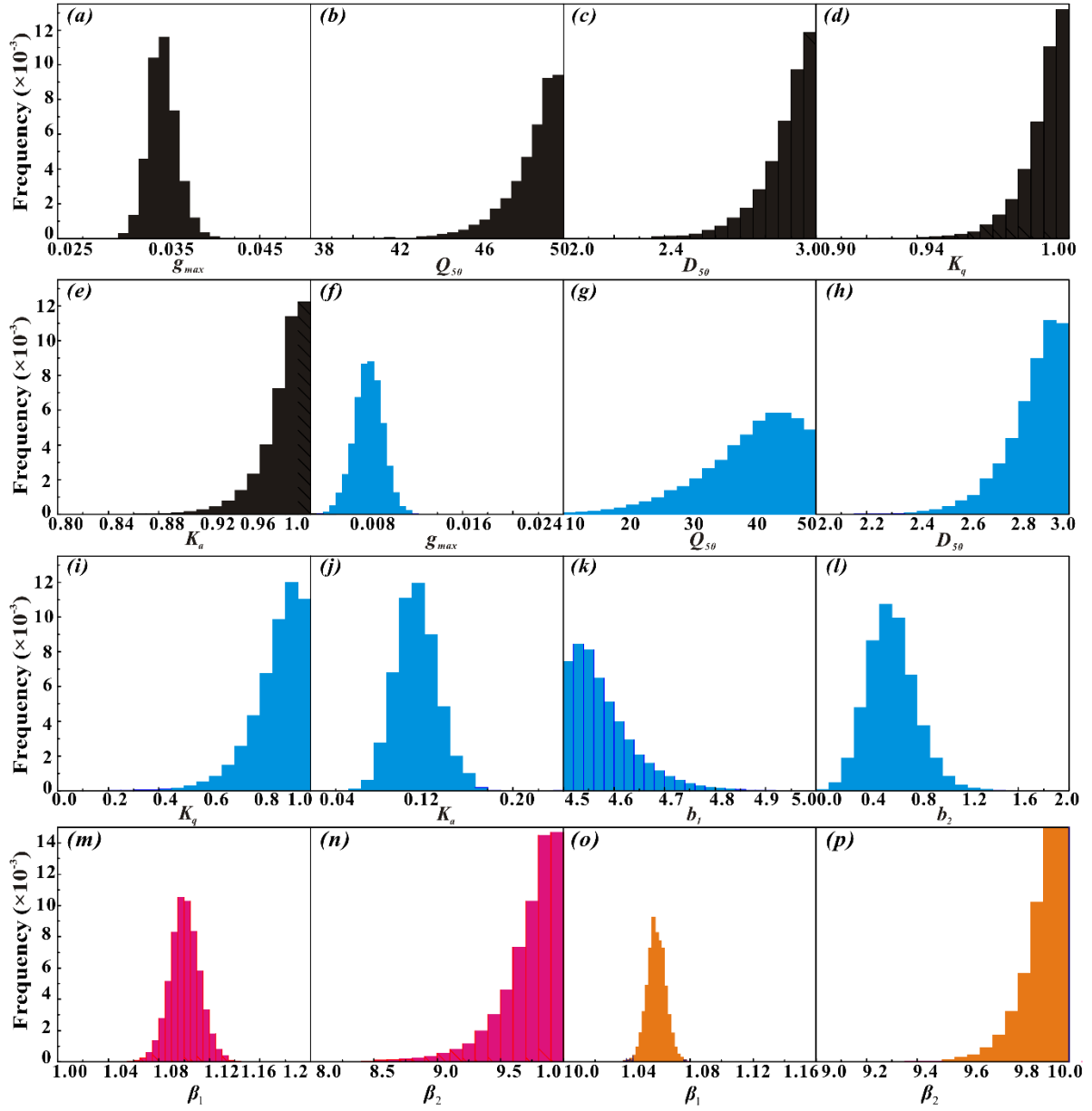


795

796 **Figure 1** Trace plots of the G-R statistic of Gelman and Rubin (Gelman and Rubin, 1992) using DREAM
 797 for the PM model (a) and (b) the SW model. Different parameters are coded with different colors. The
 798 dashed line denotes the default threshold used to diagnose convergence to a limiting distribution.

799

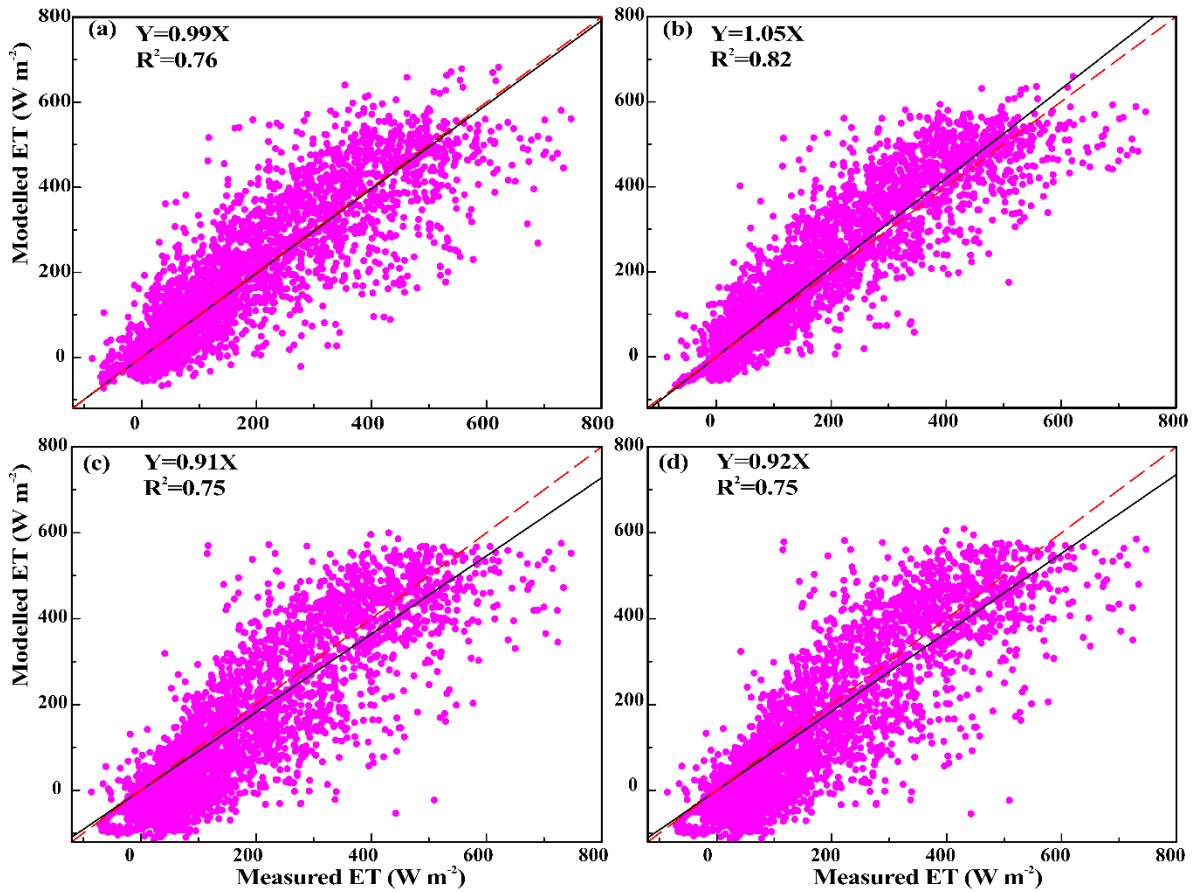
800



801

802 **Figure 2** (a)-(e), (f)-(l), (m)-(n), and (o)-(p) show histograms for the PM (black), SW (cyan), PT-FC
 803 (magenta) and AA (orange) models, respectively. These histograms are constructed from all chains for each
 804 model and a total of $40,000 \times N$ realizations are simulated using DREAM. The x axes represent the
 805 prespecified limits of the parameters.

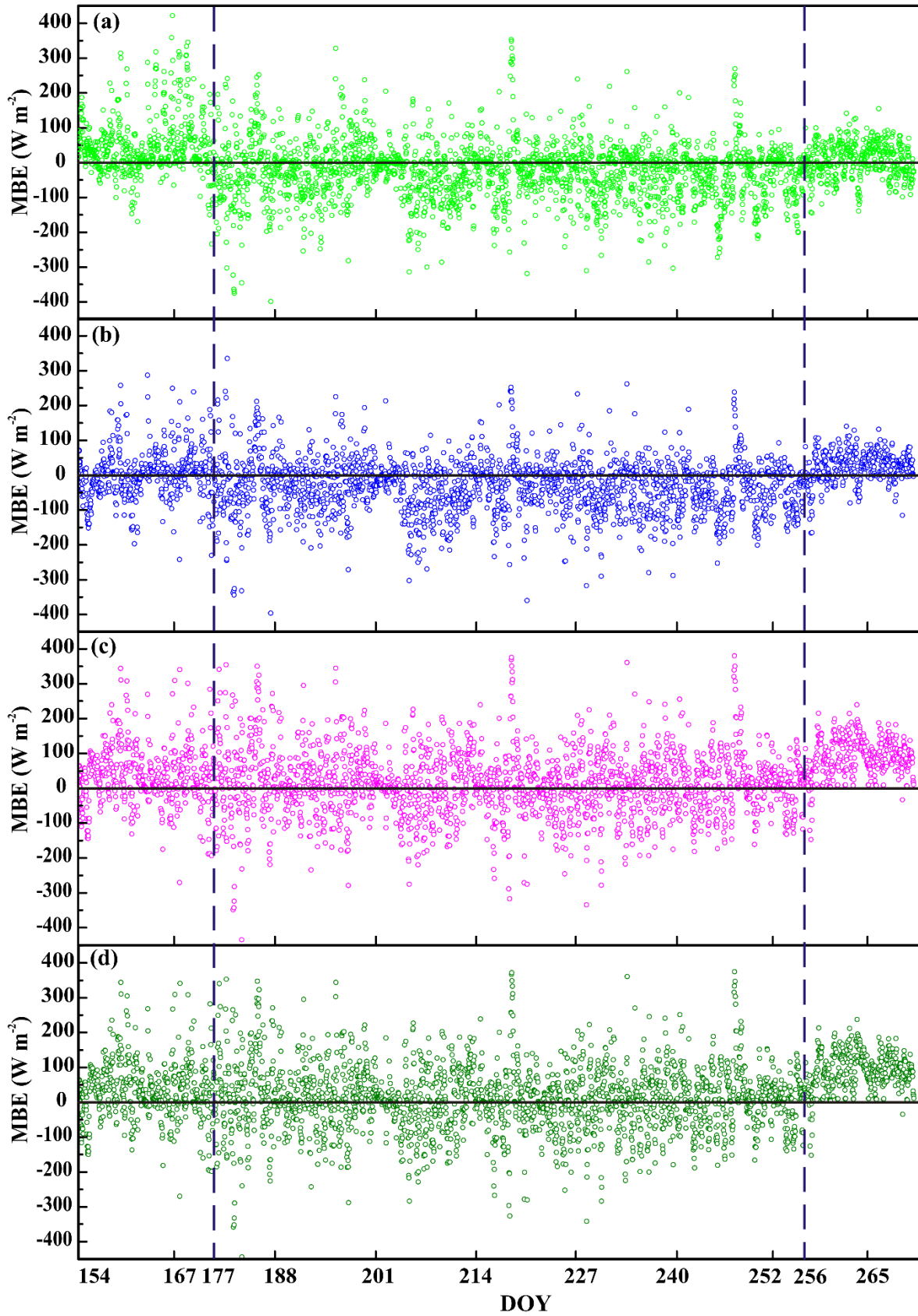
806



807

808 **Figure 3** Regressions between measured and modeled half-hourly ET values produced by different models
 809 from DOY 154 to DOY 270: (a) PM, (b) SW, (c) PT-FC and (d) AA. The regressions are: $Y = 0.99X$ ($R^2 =$
 810 0.76), $Y = 1.05X$ ($R^2 = 0.82$), $Y = 0.91X$ ($R^2 = 0.75$), and $Y = 0.92X$ ($R^2 = 0.75$) for the PM, SW, PT-FC
 811 and AA models, respectively.

812

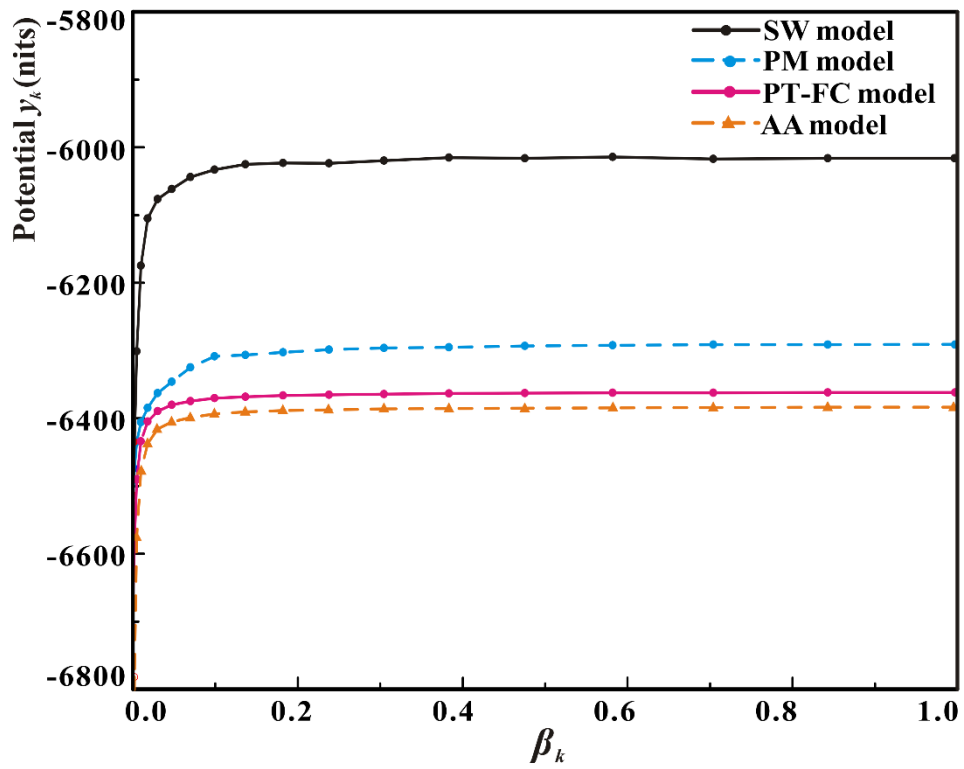


813

814 **Figure 4** Mean bias error (MBE) of predicted and observed ET values for (a) PM, (b) SW, (c) PT-FC and
 815 (d) AA models from DOY 154 to DOY 270. Parameters used for prediction are estimated by DREAM with

816 the dataset for the calibration period from DOY 154 to DOY 202.

817



818

819 **Figure 5** Variation of the mean posterior expectation of the potential y_k with β_k for the PM, SW, PT-FC and
820 AA models.

821